

Pore-Edge Tailoring of Single Atomic Iron–Nitrogen Sites on Graphene for Enhanced CO₂ Reduction

Fuping Pan,^{1,6} Boyang Li,^{2,6} Erik Sarnello,³ Yuhuan Fei,⁴ Xuhui Feng,¹ Yang Gang,¹ Xianmei

Xiang,¹ Lingzhe Fang,³ Tao Li,^{3,5} Yun Hang Hu,⁴ Guofeng Wang,^{2*} Ying Li^{1*}

¹ J. Mike Walker '66 Department of Mechanical Engineering, Texas A&M University, College Station, Texas, 77843, United States

² Department of Mechanical Engineering and Materials Science, University of Pittsburgh, Pittsburgh, Pennsylvania, 15261, United States

³ Department of Chemistry and Biochemistry, Northern Illinois University, DeKalb, Illinois 60115, United States

⁴ Department of Materials Science and Engineering, Michigan Technological University, Houghton, Michigan 49931, United States

⁵ Chemistry and Material Science Group, X-ray Science Division, Argonne National Laboratory, Lemont, Illinois 60439, United States

⁶ F.P. and B.L. contributed equally to this work.

* Corresponding author emails: guw8@pitt.edu (G.W.), yingli@tamu.edu (Y.L.)

Abstract

Hosting atomically dispersed nitrogen-coordinated iron sites (Fe–N₄) on graphene offers unique opportunities for driving electrochemical CO₂ reduction reaction (CO₂RR) to CO. However, the strong adsorption of *CO on the Fe–N₄ site embedded in intact graphene limits current density due to slow CO desorption process. Herein, we report how the manipulation of pore edges on graphene alters the local electronic structure of isolated Fe–N₄ sites and improves their intrinsic reactivity for prompting CO generation. We demonstrate that constructing holes on graphene basal plane to support Fe–N₄ can significantly enhance its CO₂RR activity as compared to the pore-deficient graphene supported Fe–N₄ counterpart, exhibiting a CO Faradaic efficiency of 94% and a turnover frequency of 1630 h⁻¹ at 0.58 V *vs.* RHE. Mechanistic studies reveal that the incorporation of pore edges results in the downshifting of the d-band center of Fe sites, which weakens the strength of Fe–C bond when *CO intermediate adsorbs on edge-hosted Fe–N₄, thus boosting the CO desorption and evolution rate. These findings suggest that engineering local support structure renders a way to design high-performance single atomic catalysts.

Keywords: local carbon structure, single-atom catalyst, pore edge, CO adsorption, CO₂ reduction

INTRODUCTION

Electrochemical CO₂ reduction offers a sustainable approach to the production of value-added fuels and chemicals by utilizing CO₂, water, and renewable energy as inputs. The electrocatalysts for CO₂ reduction reaction (CO₂RR) is at the heart of this technology because CO₂RR suffers from many inherent challenges, including sluggish kinetics, multiple reaction routes, and competition with parasitic hydrogen evolution reaction (HER) in the aqueous electrolyte.¹⁻³ Noble metal-based, for example, Au and Ag, show enhanced activity and selectivity for reducing CO₂ to CO thanks to their favorable intrinsic reactivity to CO₂ activation and weak CO adsorption;⁴⁻⁵ nevertheless, the drawbacks of prohibitive cost and limited reserves hinder their large-scale implementation.

Recently, atomically dispersed transition metals supported on nitrogen-doped carbon (M-N-C) have been exploited as promising non-precious electrocatalysts for reducing CO₂ to CO.⁶⁻¹¹ In M-N-C, nitrogen coordinated single-atom metals (M-N_x) moieties are suggested to be catalytically active sites, and carbon acts as the support in hosting N dopants and stabilizing monodispersed metal atoms.^{6, 8, 11} Despite significant advancements in designing M-N-C for CO₂RR, there still exists a big gap for commercialization due to unsatisfactory performance, limited knowledge of catalytic mechanisms, and lacking general catalysts design principles. Typically, graphene oxide (GO) has been widely employed as suitable precursor support to fabricate Fe-N₄ embedded in the graphene matrix (Fe-N-G) due to the enhanced electrostatic interaction between oxygen-containing groups on GO and Fe ions,¹²⁻¹⁴ which affords stabilizing effects to anchor isolated Fe atoms. Nonetheless, although Fe-N-G exhibited relatively small overpotentials for CO generation, it commonly delivered a moderate CO

Faradaic efficiency (FE) below 80% and a low partial current density less than 2 mA cm^{-2} ,^{8, 12} far away from the benchmark required in practical application.

In CO_2 -to-CO electroreduction, the activation of CO_2 is initiated via a proton-coupled electron transfer (PCET) process, forming the adsorbed $^*\text{COOH}$ intermediate.¹⁵⁻¹⁶ The subsequent dissociation of $^*\text{COOH}$ yields the adsorbed $^*\text{CO}$ intermediate and H_2O , which is followed by the desorption of $^*\text{CO}$ resulting in the generation of final gaseous CO. The activity of catalysts is thus strongly correlated to the adsorption strength of $^*\text{COOH}$ and $^*\text{CO}$ on catalytic sites. Based on Sabatier principle,¹⁷⁻²⁰ an ideal catalyst should have the binding energy of key intermediates that is neither too strong nor too weak to enable both reduced activation barriers and high generation rate of the targeted product. Previous theoretical and experimental investigation demonstrates that $\text{Fe}-\text{N}_4$ site located in the bulk of graphene basal plane possesses moderate adsorption with $^*\text{COOH}$, thus giving rise to low energy barrier for CO_2 activation, a potential-limiting step, and enabling small overpotentials.^{13, 19} However, the drawback of graphene bulk-hosted $\text{Fe}-\text{N}_4$ site is that it adsorbs $^*\text{CO}$ too strong, resulting in poor partial current due to the slow CO desorption process, a non-Faradaic step in CO_2RR (**Figure 1a**). It has been shown that the interaction between adsorbates and single-atom metals is determined largely by the local electronic properties of metals.²¹⁻²³ Thereby, modulating the electronic structure of $\text{Fe}-\text{N}_4$ could be a viable route to tune its electrocatalytic CO_2RR behaviors for enabling a facile CO desorption.

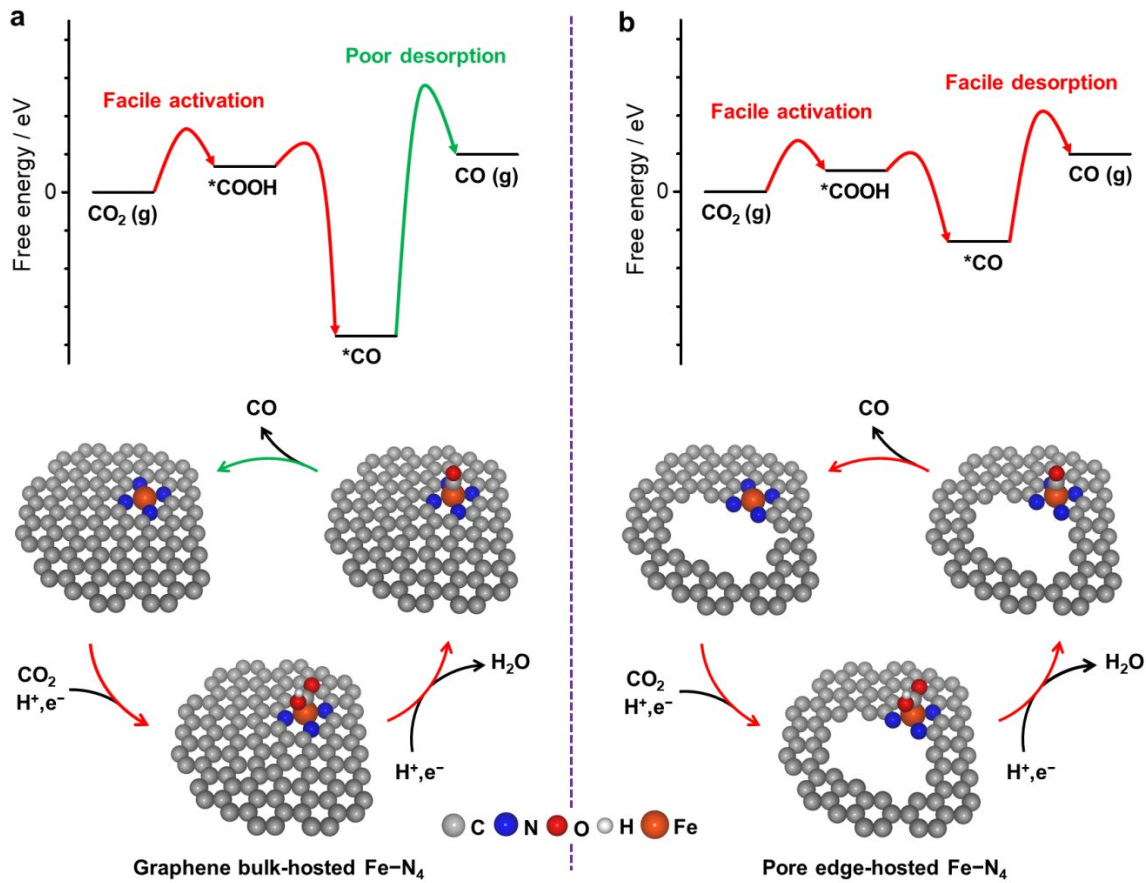


Figure 1. Schematic showing the electrocatalytic CO₂ reduction behaviors on pore-deficient graphene bulk-supported Fe-N₄ (a) and pore-rich graphene-supported Fe-N₄ (b).

As is known, the geometric structure of catalysts affects the local electronic environments of metal sites.^{22, 24-25} For example, the metal sites located at the corner, edge, and curved locations commonly possess extraordinarily intrinsic reactivity as compared to those located at the basal plane.^{21, 23, 24} Inspired by this, we sought to tailor CO₂ reduction of atomically dispersed Fe-N₄ on Fe-N-G via creating pore edges on graphene basal plane (**Figure 1b**). With anchoring Fe-N₄ on porous graphene (Fe-N-G-p), the roles of pore edges on the electronic properties and CO₂RR

behaviors of Fe–N₄ were systematically investigated. It was discovered that Fe-N-G-p can achieve highly active and selective electroreduction of CO₂ to CO, significantly outperforming pore-deficient Fe-N-G with turnover frequency (TOF) on Fe-N-G-p three times larger than that on Fe-N-G for CO generation. Theoretical modeling suggests that locating Fe–N₄ on pore edge downshifts the d-band center of Fe sites, increases the length and weakens the strength of Fe–C bond in the CO adsorption configuration as compared to Fe–N₄ embedded in the graphene bulk, thus facilitating the CO desorption and promoting CO generation.

RESULTS AND DISCUSSION

Synthesis of single atomic Fe-N-G-p

Graphene oxide (GO) was selected as a starting material to load Fe–N₄ because it has a low edge-to-bulk atom ratio due to its large sheet size up to square micrometers,²⁶ which makes GO-derived graphene a suitable reference support to identify effects of pores on CO₂ reduction by comparing with porous GO-derived graphene-supported Fe–N₄. The preparation of Fe-N-G-p involves three steps, as schematically described in **Figure 2a**. First, GO was subjected to H₂O₂ etching. Previous studies have demonstrated that H₂O₂ could act as an etchant in eroding the carbon atoms, generating nanopores throughout the basal plane of GO (GO-p).²⁷⁻²⁹ Secondly, GO-p was used as a support to adsorb Fe³⁺. Due to the enhanced interaction between oxygen groups of GO-p and Fe³⁺ ions, oxygen groups can serve as location sites to host Fe³⁺ (Fe³⁺-GO-p).^{8, 12} Thirdly, Fe³⁺-GO-p was nitrogenated at high-temperature with urea, during which the reaction between oxygen groups on Fe³⁺-GO-p and N-containing gases from the decomposition of urea reduces GO-p to porous graphene and dope N atoms

into the carbon lattice,³⁰⁻³¹ resulting in the final Fe-N-G-p catalyst. As a reference, pore-free Fe-N-G was prepared using the same procedure as to Fe-N-G-p except replacing H_2O_2 with H_2O in the first step (Figure S1a), and Fe-free N-G and N-G-p were fabricated by omitting Fe source in the second step.

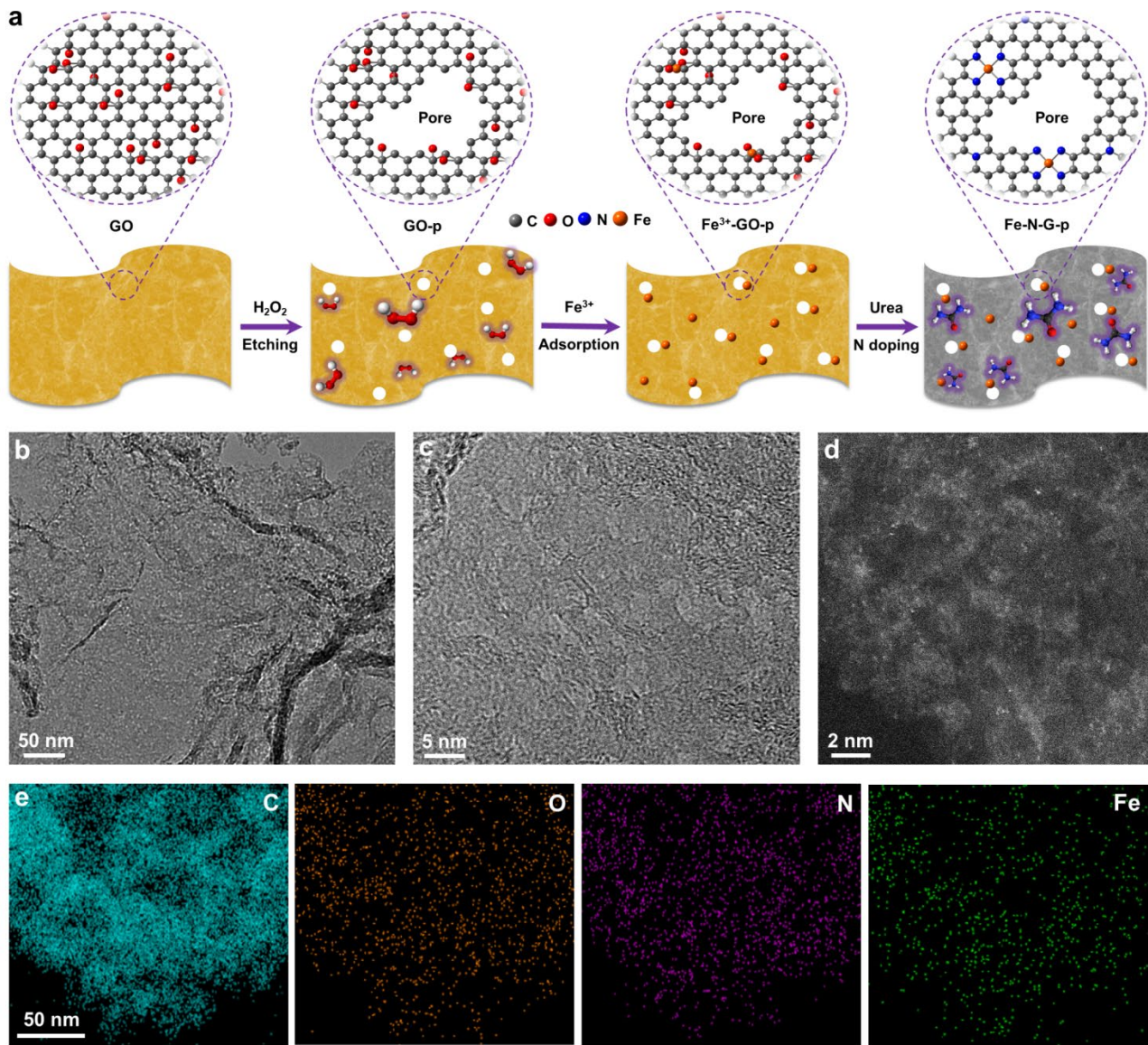


Figure 2. (a) Illustration of the preparation process for Fe-N-G-p. (b,c) TEM images, (d) HAADF-STEM image, and (e) EDS elemental mapping images of Fe-N-G-p.

Figure 2b shows that Fe-N-G has a two-dimensional flake-like feature with wrinkles, a typical N-G morphology.³² Moreover, abundant through-plane pores with sizes ranging from 2 to 5 nm were observed (**Figure 2c**), indicating the successful construction of abundant holes on the graphene nanosheets. With regard to Fe-N-G, it exhibits a similar flake-like crumpled feature but the absence of pores (Figure S1b-d), indicating the critical roles of H₂O₂ in etching graphene to create holes. HAADF-STEM image shows individual bright dots (**Figure 2d**), indicative of atomically dispersed Fe embedded in the carbon matrix. Notably, it can be seen that the isolated Fe atoms locate at both the bulk of graphene layer and the edge of holes. Elemental mapping images further confirm the dispersion of N and Fe on the graphene framework (**Figure 2e**). X-ray diffraction (XRD) patterns indicate that the two catalysts display similar carbon (002) and (101) planes at 25° and 44° with broad peaks (**Figure 3a**), implying that they are dominated by polycrystalline carbon without metallic phases. From Raman spectra (Figure S2a), two peaks at 1350 cm⁻¹ (D band) and 1590 cm⁻¹ (G band) were observed, along with close I_D/I_G ratios around 1.26 for Fe-N-C and Fe-N-G-p. This observation suggests that creating pores on GO does not induce more defects on Fe-N-G-p, which is consistent with previous reports that introducing pores on graphitic carbon and graphene oxide followed by high-temperature treatment cannot significantly affect their defective degree.³³⁻³⁴ The reason might be because the high-temperature treatment helps to repair the integrity of six-membered carbon rings that may be broken during the pore creation process. Moreover, we noted that Fe-containing catalysts showed similar I_D/I_G ratios as compared to Fe-free catalysts, probably due to the low amount of Fe

which has an insignificant influence on the defects of N-G.³⁵ According to Raman and TEM results, it can be concluded that Fe-N-G-p has pore-rich feature, not defect-rich feature, as compared to Fe-N-G.

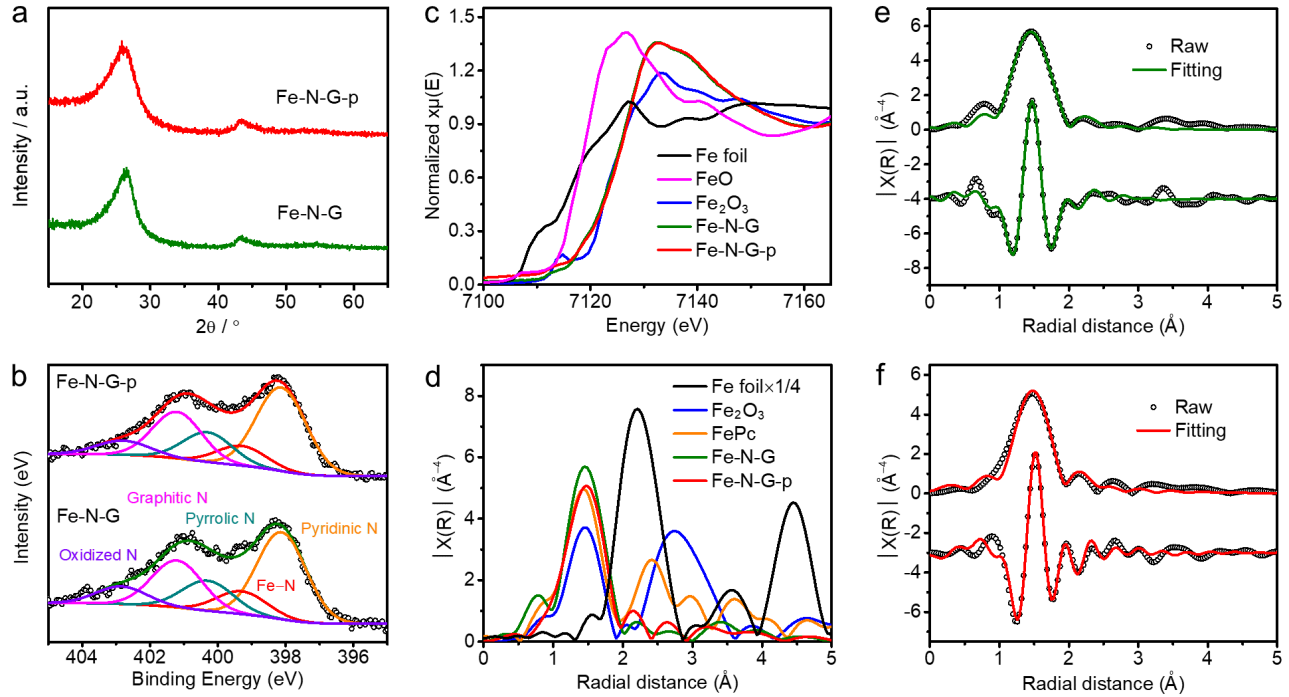


Figure 3. (a) XRD patterns, (b) N 1s XPS, (c) XANES, (d) EXAFS, (e,f) Fitting of EXAFS spectra for Fe-N-G and Fe-N-G-p.

Characterization of composition and structure

X-ray photoelectron spectroscopy (XPS) survey spectra show obvious C, N, O peaks (Figure S3a); no obvious Fe signal in survey spectra was attributed to their low contents. The loading amount of Fe was quantified to be 0.36 and 0.44 wt% in Fe-N-G-p and Fe-N-G by inductively coupled plasma mass spectrometry (ICP-MS), respectively, which are within the range of values reported in the literature.³⁶

The total atomic N contents were measured to be around 8 at% (Figure S3b), and the fitting of N 1s spectra reveals the formation of pyridinic N (398.1 eV), Fe–N (399.3 eV), pyrrolic N (400.3 eV), graphitic N (401.2 eV), and oxidized N (402.8 eV).³⁷⁻³⁹ It is noting that Fe-N-G and Fe-N-G-p displayed similar percentages for these N species (Table S1), suggesting that the construction of holes on graphene does not impact much on N contents and their local configurations.

To capture more information on chemical environments and atomic coordination, X-ray absorption spectroscopy (XAS) were performed; Fe foil, iron phthalocyanine (FePc), FeO, and Fe₂O₃ were also tested as standard references. **Figure 3c** depicts X-ray absorption near edge structure (XANES) spectra, in which the absorption features of the pre-edge and edge correspond to 1s → 3d and 1s → 4p transition, respectively.³⁹ Both Fe-N-G and Fe-N-G-p showed the pre-edge and edge shift at 7114 and 7125 eV, respectively, close to those of Fe₂O₃ but largely different from FeO and Fe foil (Figure S4). These results confirm that the oxidization state of Fe in the catalysts is dominantly in Fe³⁺. In addition, the intensity of the pre-edge peak has been suggested to be dependent on the site symmetry, and a lower intensity means a higher symmetry of Fe site.³⁹ Here, Fe-N-G-p exhibited a slightly higher pre-edge intensity than Fe-N-G, implying a weaker symmetry of Fe site on Fe-N-G-p. The observation might be as a result of the pores on Fe-N-G-p layer that may cause slight local spatial distortion from the square planar symmetry, as compared to pore-deficient Fe-N-G.

Fourier transform (F-T) extended X-ray absorption fine structure (EXAFS) was further analyzed. Fe-N-G and Fe-N-G-p show obvious peaks at 1.5 Å (**Figure 3d**), which can be ascribed to the Fe–N(O) coordination, consistent with the radial distance of Fe–N and Fe–O present in FePc and Fe₂O₃,

respectively. Notably, there is no peak of Fe–Fe positioned at 2.2 Å for Fe-N-G and Fe-N-G-p, further confirming the monodispersing of Fe in the graphene without Fe-based aggregates. Based on the fitting results (**Figure 3e,f**, Table S2), one Fe atom more likely coordinates with four N atoms and one O atom in these two catalysts. The Fe–O signal can be attributed to the adsorption of oxygen molecule on the Fe site released from the synthesis process or from air.⁴⁰ Under the real CO₂RR condition, the adsorbed oxygen can be quickly reduced to H₂O since the thermodynamic potential of oxygen reduction is more than 1.0 V positive that of CO₂RR,⁴¹ thus leaving Fe–N₄ as the effective site for CO₂RR. These characterizations demonstrate that the creation of pores did not change the atomic coordination of isolated Fe atoms, making as-prepared catalysts ideal models to exclusively explore the influence of pore edges on intrinsic catalytic properties of Fe–N₄ for CO₂RR.

Since Fe-N-G catalyst has a large size of graphene up to micrometers and thus a low edge-to-bulk ratio, it can be inferred that atomic Fe sites are mainly embedded in the bulk of the graphene's basal plane. Regarding Fe-N-G-p, it has a large number of through-plane pores, consequently, the Fe atoms can locate at both the bulk and pore edge of the holey graphene layers. We thus constructed three moieties to represent the possible Fe–N₄ configurations, including Fe–N₄-bulk, Fe–N₄-pore, and Fe–N₄-edge (**Figure 4**). As Fe atom has been proposed to be stabilized by N dopants, we further predicted the formation energies for these three configurations by calculating the energy change for Fe atom insertion into the N-G matrix. The formation energies for Fe–N₄-pore and Fe–N₄-edge were predicted to be lower than that of Fe–N₄-bulk, implying that pore and edge locations are thermodynamically more favorable to stabilize Fe atom for Fe–N bond formation. Combining with

TEM, HAADF-STEM, and XAS characterization, it can thus be inferred that there exist Fe–N₄ sites locating at the edge position of the holey graphene layers, despite the quantification of the ratio between edge- and bulk-hosted Fe–N sites is infeasible due to the severe overlapping of Fe–N–G–p layers.

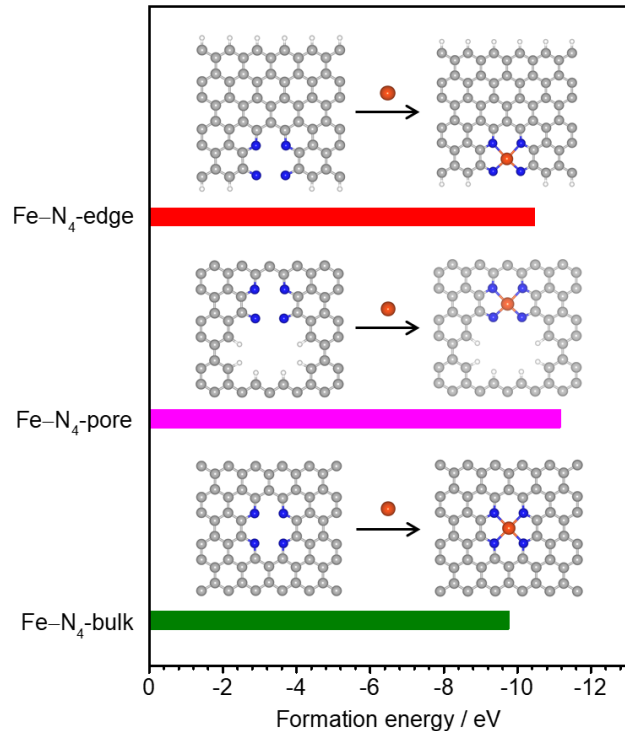


Figure 4. Calculated formation energy for proposed Fe–N₄-bulk, Fe–N₄-pore, and Fe–N₄-edge sites.

The gray, blue, red, orange, and white balls refer to carbon, nitrogen, oxygen, iron, and hydrogen atoms, respectively.

Evaluation of CO₂ reduction activity

Having pore-deficient Fe–N–G and pore-rich Fe–N–G–p as model catalysts with Fe-free N–G and N–G–p as controls, their electrochemical properties toward CO₂ reduction were evaluated in CO₂-saturated KHCO₃ solution. **Figure 5a** presents CO FEs at different potentials. The FEs on N–G–p are

very close to those of N-G in the whole potential range, suggesting that pores do not impact much on the catalytic reactivity of N dopants. Notably, Fe-N-G-p exhibited larger CO FEs in the entire potential region than N-G, N-G-p, and Fe-N-G, delivering a maximum CO FE of 94% at -0.58 V, 13% higher relative to Fe-N-G, indicating that the incorporation of pores increases the catalytic CO generation selectivity over Fe-N₄. Previous theoretical predictions have demonstrated that the catalytic selectivity of M-N-C depends highly on the configurations of M-N_x moieties and local carbon support structure,⁴²⁻⁴⁴ which could reduce CO₂ to deep reduction products such as CH₄ and CH₃OH. In our case, CO is the main product from CO₂RR over Fe-N₄, in a good agreement with reported experimental findings (Table S3). No deep reduction products might be because there requires a very large overpotential around 1.0 V to further reduce CO to *CHO on Fe-N₄, at which HER becomes dominant and suppresses CO₂RR. No C₂₊ products can be attributed to the absence of neighboring Fe atoms ensembles in atomically dispersed Fe-N-G-p, which is necessary to enable C-C coupling via *CO dimerization for C₂₊ formation.⁴⁵

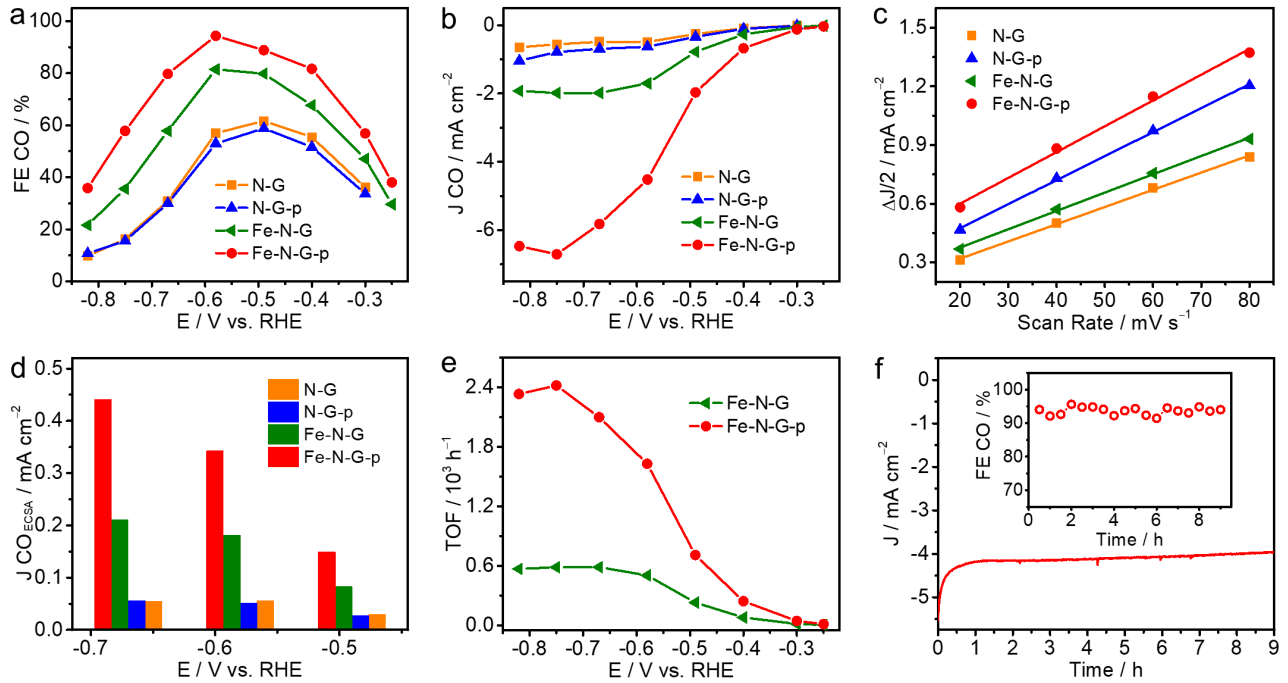


Figure 5. Electrochemical CO₂ reduction activity. (a) CO FEs, (b) CO partial current density, (c) ECSA measurements, (d) CO current normalized by C_{dl} for N-G, N-G-p, Fe-N-G, and Fe-N-G-p. (e) TOF per Fe site for CO generation. (f) stability test at -0.58 V for Fe-N-G-p.

Figure 5b shows that Fe-containing catalysts possessed significantly larger CO partial current density than N-G and N-G-p, along with the enhanced FEs (**Figure 5b**), suggesting that single-atom Fe–N₄ serves as the primary catalytic sites.^{10, 35} In addition, currents of N-G-p are slightly larger relative to those of N-G, while Fe-N-G-p exhibited substantially higher currents than Fe-N-G, further confirming the minor influences of pores on N dopants but considerable effects on Fe–N₄. In specific, Fe-N-G-p had a CO partial current density of 4.5 mA cm⁻² at -0.58 V, more than two times larger than 1.7 mA cm⁻² of Fe-N-G. These results manifest that locating atomically dispersed Fe–N₄ on

holey graphene can improve electrocatalytic CO_2 reduction performance in comparison with pristine graphene support. Moreover, activity of Fe-N-G-p is comparable to that achieved on state-of-the-art Fe-N-C (Table S3), such as Fe,N-doped porous carbon derived from polymer,¹⁵ Fe-N-doped graphene prepared via pyrolysis of g- C_3N_4 and glucose,³⁵ and Fe-N-doped porous carbon nanoparticles derived from ZIF.⁴⁶ Given that GO-derived Fe-N-G commonly shows poor CO_2RR ,^{8, 12} the proposed pore-engineering approach opens up opportunities for the use of low-cost GO to fabricate high-efficiency Fe-N-C toward CO_2 electroreduction.

To accurately examine the intrinsic reactivity, we determined the electrochemical active surface area (ECSA), being 8.8, 12.3, 9.4, 13.2 mF cm^{-2} for N-G, N-G-p, Fe-N-G, and Fe-N-G-p, respectively (**Figure 5c**, Figure S5). The improved values on porous catalysts suggest that pores contribute to the enhancement in the accessibility of active sites. The ECSA-normalized CO currents of Fe-N-G-p are remarkably larger relative to those of Fe-N-G, while there is no obvious difference of ECSA-normalized currents between N-G and N-G-p. TOF per Fe site for CO generation was further calculated (**Figure 5e**), in which Fe-N-G-p showed significantly larger TOF than Fe-N-G in the all potential range. For instance, Fe-N-G-p exhibited a TOF of 1630 h^{-1} at -0.58 V , more than three times larger than 504 h^{-1} of Fe-N-G, implying the considerably faster CO production rate per Fe site on Fe-N-G-p than Fe-N-G. From Nyquist plots (Figure S6), it was found that the charge-transfer resistance (R_{CT}) slightly decreases from 24.3Ω on Fe-N-G to 19.7Ω on Fe-N-G-p, suggesting that pores do not contribute much in lowering the charge-transfer resistance. Moreover, both Fe-N-G and Fe-N-G-p show close Tafel slopes of near 118 mV dec^{-1} , suggesting that CO_2RR proceeds through a

similar mechanism involving PCET-assisted CO_2 activation to $^*\text{COOH}$ (Figure S7).⁴⁷ In view of these electrochemical results, it can be concluded that the pore edges play pivotal roles in enhancing the inherent activity and selectivity of $\text{Fe}-\text{N}_4$ sites on the graphene bulk for catalyzing CO_2 reduction to CO . Moreover, $\text{Fe}-\text{N}-\text{G}-\text{p}$ can preserve FEs and current in a 9 h continuous electrolysis (**Figure 5f**), suggesting enhanced electrochemical CO_2 reduction durability.

Elucidation of pore edge's roles by DFT calculation

To gain further insight into the observed pore-engineering effects, density functional theory (DFT) calculations were carried out on $\text{Fe}-\text{N}_4$ -bulk, $\text{Fe}-\text{N}_4$ -pore, and $\text{Fe}-\text{N}_4$ -edge (**Figure 4**). COOH^* and CO^* were considered to be intermediates involved in CO_2RR through a PCET mechanism (**Figure 6a**, Figure S8).^{35, 47-48} **Figure 6b** shows that the first PCET process for the activation of CO_2 to $^*\text{COOH}$ is the potential-limiting step due to its thermodynamically uphill nature, thus determining the onset potential of CO_2RR . This result is consistent to the predictions from explicit solvation model calculations on $\text{Cu}(111)^{49}$ and Cu (211) surface⁵⁰⁻⁵¹ for CO_2 reduction to CO . Moreover, a weak CO adsorption can lead to a large CO flux, hence the last CO desorption step, a non-Faradaic step, could determine the final CO generation rate (partial current density). The CO adsorption energy is defined as the free energy difference between the adsorbed CO and free molecule CO .^{15, 52} Our DFT results show that $\text{Fe}-\text{N}_4$ -bulk site exhibited a limiting potential of 0.42V and a CO adsorption energy of -1.06 eV. In comparison, the introduction of pore edge in graphene is predicted to lower the limiting potential to 0.29 and 0.30 V and weaken the CO adsorption energy to -0.92 and -0.72 eV on $\text{Fe}-\text{N}_4$ -pore and $\text{Fe}-\text{N}_4$ -edge, respectively. These results suggest that pore-edge decoration could slightly

decrease the onset potential of CO₂RR and significantly boost the CO desorption. This explains our experimental results that TOF on Fe-N-G-p is more than three times larger than that on Fe-N-G (**Figure 4e**). HER is a competitive reaction in CO₂RR, and the difference of limiting potential ($U_L(\text{CO}_2) - U_L(\text{H}_2)$) was calculated to gauge the selectivity of CO₂RR, a more positive value indicative of better selectivity to CO generation.^{35, 53-54} As depicted in **Figure 6c**, Fe-N₄-pore and Fe-N₄-edge sites exhibited $U_L(\text{CO}_2) - U_L(\text{H}_2)$ values of 0.23 and 0.18 V, respectively, larger or similar than that of Fe-N₄-bulk (0.18 V). This indicates that the introduction of pore could increase CO selectivity, in good agreement with larger FEs of CO observed on Fe-N-G-p.

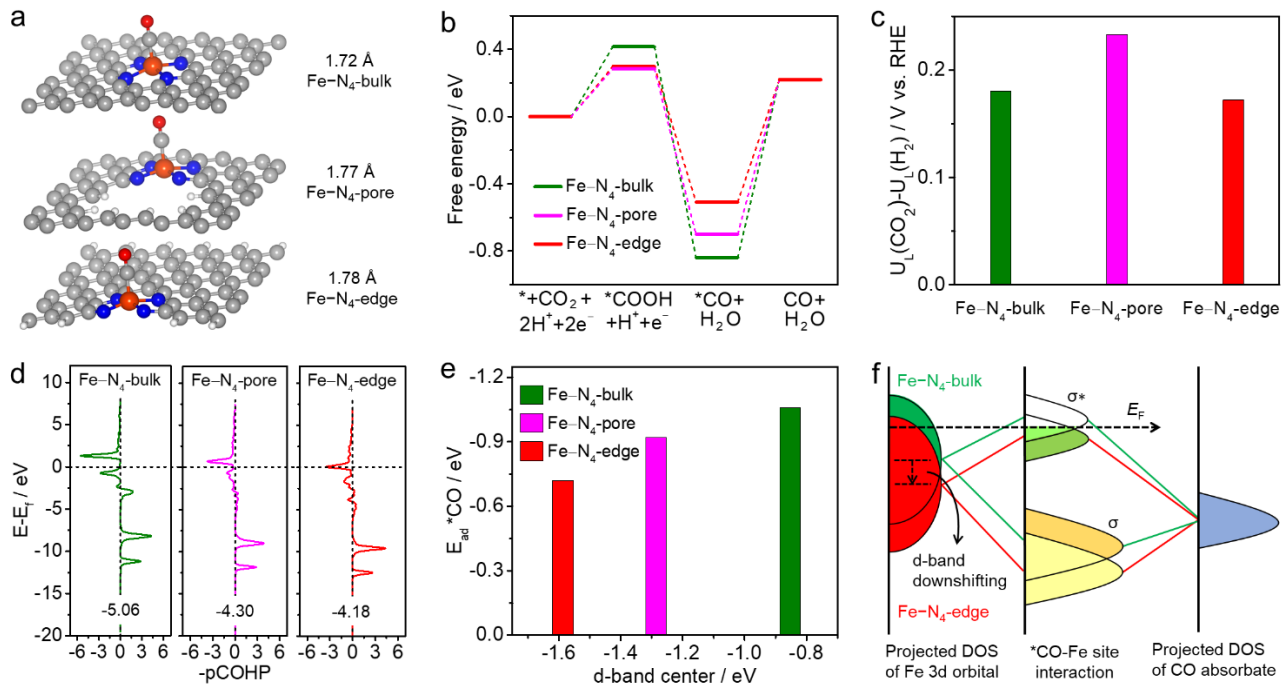


Figure 6. (a) Atomic configurations of *CO adsorbed on different Fe-N₄ moieties and the length of Fe-C bond in the OC-Fe-N₄ configuration. The gray, blue, red, orange, and white balls represent carbon, nitrogen, oxygen, iron, and hydrogen atoms, respectively. (b) Free energy diagrams of CO₂RR

at $U=0$ V. (c) Calculated difference limiting potentials for CO_2RR and HER. (d) Projected COHP analysis, (e) Correlation between the d-band center of single Fe sites and adsorption energy of $^*\text{CO}$. (f) Scheme showing bond formation between atomic Fe sites and CO adsorbate on $\text{Fe}-\text{N}_4\text{-bulk}$, $\text{Fe}-\text{N}_4\text{-pore}$, $\text{Fe}-\text{N}_4\text{-edge}$ models.

The electronic properties were analyzed to unveil the roles of pore edge in influencing CO adsorption on $\text{Fe}-\text{N}_4$. In the dissociation of $^*\text{COOH}$ to $^*\text{CO}$, the length of Fe–C bond on $\text{Fe}-\text{N}_4\text{-bulk}$, $\text{Fe}-\text{N}_4\text{-pore}$, and $\text{Fe}-\text{N}_4\text{-edge}$ sites are 1.72, 1.77, and 1.78 Å (**Figure 6a**), respectively. The increase in the length of Fe–C bond suggests a weaker $^*\text{CO}$ adsorption on edge-rich sites, which agrees with the empirical conclusion that a stronger interaction will result in a shorter bond. The crystal orbital Hamilton population (COHP) analysis, in which the interaction between the two orbitals of adjacent atoms is described by the project of DOS and Hamilton matrix, was also employed to evaluate the bonding strength.⁵⁵ In **Figure 6d**, the negative section of x-axis presents the anti-bonding strength of Fe–C bond, whereas the positive section refers to the bonding strength. Therefore, we could estimate the bonding strength of Fe–C by integrating the projected COHP below Fermi energy (E_f). The integrated -pCOHP of Fe–C bond was predicted to be -5.06, -4.30, and -4.18 eV on $\text{Fe}-\text{N}_4\text{-bulk}$, $\text{Fe}-\text{N}_4\text{-pore}$, and $\text{Fe}-\text{N}_4\text{-edge}$, respectively, further indicating that the interaction of $^*\text{CO}$ and $\text{Fe}-\text{N}_4$ becomes weaker on pore-rich sites as compared to pore-free sites.

Moreover, we carried out density of state (DOS) analysis to obtain the d-band center of Fe, an important indicator to describe the electronic interaction between adsorbate and metal center (Figure

S9). The d-band center was estimated to be -0.92 , -1.29 , -1.52 eV on Fe–N₄-bulk, Fe–N₄-pore, and Fe–N₄-edge (**Figure 6e**), respectively, suggesting that pore engineering results in the downshifting of d-band center of Fe site. The positive correlation between CO adsorption energy and d-band center implies that the pore edge-induced down-shifting of the d-band center mainly accounts for the weakening of CO adsorption on the single Fe site. Based on these computational results, we proposed a schematic to illustrate the bond formation between CO adsorbate and Fe–N₄ (**Figure 6f**). Upon introducing pores on graphene basal plane, the d-band center of Fe center of Fe–N₄ becomes lower away from the E_f. As the antibonding state is known to be above the d states,⁵⁶ there is thus an increase in the electron occupation of anti-bonding orbitals on edge-rich Fe–N₄ as compared to the edge-free counterpart. Thereby, the pore-edge modification decreases the adsorption energy of *CO, which boosts the desorption of *CO from Fe-N-G-p surface and leave more fresh sites promoting CO generation. Accordingly, DFT results manifest that CO₂-to-CO electroreduction on single atomic Fe–N₄ can be effectively regulated by tailoring the d-band center of Fe site through pore-edge engineering.

CONCLUSIONS

Combining both experimental and theoretical analyses, we demonstrate that electronic properties and electrocatalytic CO₂ reduction behaviors of graphene supported atomically dispersed Fe–N₄ can be modulated by constructing pores on graphene basal plane. Compared to graphene bulk-supported Fe–N₄, locating Fe–N₄ on pore edge of graphene can downshift the d-band center of Fe atom. This electronic modification weakens the adsorption of *CO intermediate on pore-hosted Fe–N₄ sites via

increasing the length and decreasing the strength of Fe–C bond in the CO adsorption configuration, thus facilitating the *CO desorption process. Using holey graphene-anchored Fe–N₄ as a catalyst, a high FE of 94% and a TOF of 1630 h⁻¹ for CO generation were achieved at 0.58 V, surpassing the pore-free graphene-supported counterpart (81%, 504 h⁻¹). The findings provide insights on how catalytic reactivity of atomic metal can be tuned by engineering pore-edge structure of carbon support, offering a direction to design advanced carbon-supported single-atom electrocatalysts for a broad spectrum of electrocatalysis.

AUTHOR INFORMATION

Corresponding Author

* Email: guw8@pitt.edu (G.W.), yingli@tamu.edu (Y.L.)

Notes

The authors declare no competing financial interest.

SUPPORTING INFORMATION

The Supporting Information is available free of charge at the ACS Publications website Catalysts synthesis, catalysis characterizations, electrochemical measurements, computational methods, additional results of CO₂RR activity, and performance comparison.

ACKNOWLEDGMENTS

Y.L. and G.W. thanks the financial support from U.S. National Science Foundation (NSF CBET #1805132, #1804534, #ACI-1053575). T. Li thanks NIU startup support. The use of Materials Characterization Facility (MCF) at Texas A&M University, computational resources at University of

Pittsburgh Center for Research Computing and the Extreme Science and Engineering Discovery Environment (XSEDE), Advanced Photon Source and the Center for Nanoscale Materials at Argonne National Laboratory supported by the U.S. Department of Energy under Contract No. DE-AC02-06CH11357 are acknowledged.

REFERENCES

1. Birdja, Y. Y.; Pérez-Gallent, E.; Figueiredo, M. C.; Göttle, A. J.; Calle-Vallejo, F.; Koper, M. T. M., Advances and Challenges in Understanding the Electrocatalytic Conversion of Carbon Dioxide to Fuels. *Nat. Energy* **2019**, *4*, 732–745.
2. De Luna, P.; Hahn, C.; Higgins, D.; Jaffer, S. A.; Jaramillo, T. F.; Sargent, E. H., What Would it Take for Renewably Powered Electrosynthesis to Displace Petrochemical Processes? *Science* **2019**, *364*, 3506.
3. Pan, F.; Zhang, H.; Liu, Z.; Cullen, D.; Liu, K.; More, K.; Wu, G.; Wang, G.; Li, Y., Atomic-Level Active Sites of Efficient Imidazolate Framework-Derived Nickel Catalysts for CO₂ Reduction. *J. Mater. Chem. A* **2019**, *7*, 26231-26237.
4. Zhu, W.; Zhang, Y.-J.; Zhang, H.; Lv, H.; Li, Q.; Michalsky, R.; Peterson, A. A.; Sun, S., Active and Selective Conversion of CO₂ to CO on Ultrathin Au Nanowires. *J. Am. Chem. Soc.* **2014**, *136*, 16132-16135.
5. Lu, Q.; Rosen, J.; Zhou, Y.; Hutchings, G. S.; Kimmel, Y. C.; Chen, J. G.; Jiao, F., A Selective and Efficient Electrocatalyst for Carbon Dioxide Reduction. *Nat. Commun.* **2014**, *5*, 3242.

6. Zheng, T.; Jiang, K.; Wang, H., Recent Advances in Electrochemical CO₂-to-CO Conversion on Heterogeneous Catalysts. *Adv. Mater.* **2018**, *30*, 1802066.
7. Gang, Y.; Pan, F.; Fei, Y.; Du, Z.; Hu, Y. H.; Li, Y., Highly Efficient Nickel, Iron, and Nitrogen Codoped Carbon Catalysts Derived from Industrial Waste Petroleum Coke for Electrochemical CO₂ Reduction. *ACS Sustain. Chem. Eng.* **2020**, *8*, 8840-8847.
8. Zhang, C.; Yang, S.; Wu, J.; Liu, M.; Yazdi, S.; Ren, M.; Sha, J.; Zhong, J.; Nie, K.; Jalilov, A. S.; Li, Z.; Li, H.; Yakobson, B. I.; Wu, Q.; Ringe, E.; Xu, H.; Ajayan, P. M.; Tour, J. M., Electrochemical CO₂ Reduction with Atomic Iron-Dispersed on Nitrogen-Doped Graphene. *Adv. Energy Mater.* **2018**, *8*, 1703487.
9. Yan, C.; Li, H.; Ye, Y.; Wu, H.; Cai, F.; Si, R.; Xiao, J.; Miao, S.; Xie, S.; Yang, F.; Li, Y.; Wang, G.; Bao, X., Coordinatively Unsaturated Nickel-Nitrogen Sites towards Selective and High-Rate CO₂ Electroreduction. *Energy Environ. Sci.* **2018**, *11*, 1204-1210.
10. Pan, F.; Zhang, H.; Liu, K.; Cullen, D. A.; More, K. L.; Wang, M.; Feng, Z.; Wang, G.; Wu, G.; Li, Y., Unveiling Active Sites of CO₂ Reduction on Nitrogen Coordinated and Atomically Dispersed Iron and Cobalt Catalysts. *ACS Catal.* **2018**, *8*, 3116-3122.
11. Zhao, C.; Wang, Y.; Li, Z.; Chen, W.; Xu, Q.; He, D.; Xi, D.; Zhang, Q.; Yuan, T.; Qu, Y.; Yang, J.; Zhou, F.; Yang, Z.; Wang, X.; Wang, J.; Luo, J.; Li, Y.; Duan, H.; Wu, Y.; Li, Y., Solid-Diffusion Synthesis of Single-Atom Catalysts Directly from Bulk Metal for Efficient CO₂ Reduction. *Joule* **2018**, *3*, 584-594.

12. Jiang, K.; Siahrostami, S.; Zheng, T.; Hu, Y.; Hwang, S.; Stavitski, E.; Peng, Y.; Dynes, J.; Gangisetty, M.; Su, D.; Attenkofer, K.; Wang, H., Isolated Ni Single Atoms in Graphene Nanosheets for High-Performance CO₂ Reduction. *Energy Environ. Sci.* **2018**, *11*, 893-903
13. Pan, F.; Li, B.; Sarnello, E.; Fei, Y.; Gang, Y.; Xiang, X.; Du, Z.; Zhang, P.; Wang, G.; Nguyen, H. T.; Li, T.; Hu, Y. H.; Zhou, H.-C.; Li, Y., Atomically Dispersed Iron-Nitrogen Sites on Hierarchically Mesoporous Carbon Nanotubes and Graphene Nanoribbons Networks for CO₂ Reduction. *ACS Nano* **2020**, *14*, 5506–5516.
14. Fei, H.; Dong, J.; Chen, D.; Hu, T.; Duan, X.; Shakir, I.; Huang, Y.; Duan, X., Single Atom Electrocatalysts Supported on Graphene or Graphene-Like Carbons. *Chem. Soc. Rev.* **2019**, *48*, 5207–5241.
15. Ju, W.; Bagger, A.; Hao, G.-P.; Varela, A. S.; Sinev, I.; Bon, V.; Roldan Cuenya, B.; Kaskel, S.; Rossmeisl, J.; Strasser, P., Understanding Activity and Selectivity of Metal-Nitrogen-Doped Carbon Catalysts for Electrochemical Reduction of CO₂. *Nat. Commun.* **2017**, *8*, 944.
16. Geng, Z.; Kong, X.; Chen, W.; Su, H.; Liu, Y.; Cai, F.; Wang, G.; Zeng, J., Oxygen Vacancies in ZnO Nanosheets Enhance CO₂ Electrochemical Reduction to CO. *Angew. Chem. Int. Ed.* **2018**, *57*, 6054-6059.
17. Koper, M. T. M., Thermodynamic Theory of Multi-Electron Transfer Reactions: Implications for Electrocatalysis. *J. Electroanal. Chem.* **2011**, *660*, 254-260.
18. Zhang, Y.-J.; Sethuraman, V.; Michalsky, R.; Peterson, A. A., Competition between CO₂ Reduction and H₂ Evolution on Transition-Metal Electrocatalysts. *ACS Catal.* **2014**, *4*, 3742-3748.

19. Feaster, J. T.; Shi, C.; Cave, E. R.; Hatsukade, T.; Abram, D. N.; Kuhl, K. P.; Hahn, C.; Nørskov, J. K.; Jaramillo, T. F., Understanding Selectivity for the Electrochemical Reduction of Carbon Dioxide to Formic Acid and Carbon Monoxide on Metal Electrodes. *ACS Catal.* **2017**, *7*, 4822-4827.
20. Bagger, A.; Ju, W.; Varela, A. S.; Strasser, P.; Rossmeisl, J., Electrochemical CO₂ Reduction: A Classification Problem. *Chemphyschem* **2017**, *18*, 3266-3273.
21. Wang, A.; Li, J.; Zhang, T., Heterogeneous Single-Atom Catalysis. *Nat. Rev. Chem.* **2018**, *2*, 65-81.
22. Liu, D.; Li, X.; Chen, S.; Yan, H.; Wang, C.; Wu, C.; Haleem, Y. A.; Duan, S.; Lu, J.; Ge, B.; Ajayan, P. M.; Luo, Y.; Jiang, J.; Song, L., Atomically Dispersed Platinum Supported on Curved Carbon Supports for Efficient Electrocatalytic Hydrogen Evolution. *Nat. Energy* **2019**, *4*, 512-518.
23. Zhang, J.; Zhao, Y.; Chen, C.; Huang, Y.-C.; Dong, C.-L.; Chen, C.-J.; Liu, R.-S.; Wang, C.; Yan, K.; Li, Y.; Wang, G., Tuning the Coordination Environment in Single-Atom Catalysts to Achieve Highly Efficient Oxygen Reduction Reactions. *J. Am. Chem. Soc.* **2019**, *141*, 20118-20126.
24. Chen, Y.; Ji, S.; Zhao, S.; Chen, W.; Dong, J.; Cheong, W.-C.; Shen, R.; Wen, X.; Zheng, L.; Rykov, A. I.; Cai, S.; Tang, H.; Zhuang, Z.; Chen, C.; Peng, Q.; Wang, D.; Li, Y., Enhanced Oxygen Reduction with Single-Atomic-Site Iron Catalysts for A Zinc-Air Battery and Hydrogen-Air Fuel Cell. *Nat. Commun.* **2018**, *9*, 5422.
25. Liu, K.; Wu, G.; Wang, G., Role of Local Carbon Structure Surrounding FeN₄ Sites in Boosting the Catalytic Activity for Oxygen Reduction. *J. Phys. Chem. C* **2017**, *121*, 11319-11324.

26. Marcano, D. C.; Kosynkin, D. V.; Berlin, J. M.; Sinitskii, A.; Sun, Z.; Slesarev, A.; Alemany, L. B.; Lu, W.; Tour, J. M., Improved Synthesis of Graphene Oxide. *ACS Nano* **2010**, *4*, 4806-4814.
27. Sun, H.; Mei, L.; Liang, J.; Zhao, Z.; Lee, C.; Fei, H.; Ding, M.; Lau, J.; Li, M.; Wang, C.; Xu, X.; Hao, G.; Papandrea, B.; Shakir, I.; Dunn, B.; Huang, Y.; Duan, X., Three-Dimensional Holey-Graphene/Niobia Composite Architectures for Ultrahigh-Rate Energy Storage. *Science* **2017**, *356*, 599-604.
28. Xu, Y.; Lin, Z.; Zhong, X.; Huang, X.; Weiss, N. O.; Huang, Y.; Duan, X., Holey Graphene Frameworks for Highly Efficient Capacitive Energy Storage. *Nat. Commun.* **2014**, *5*, 4554.
29. Xu, Y.; Chen, C.-Y.; Zhao, Z.; Lin, Z.; Lee, C.; Xu, X.; Wang, C.; Huang, Y.; Shakir, M. I.; Duan, X., Solution Processable Holey Graphene Oxide and Its Derived Macrostructures for High-Performance Supercapacitors. *Nano Lett.* **2015**, *15*, 4605-4610.
30. Li, X.; Wang, H.; Robinson, J. T.; Sanchez, H.; Diankov, G.; Dai, H., Simultaneous Nitrogen Doping and Reduction of Graphene Oxide. *J. Am. Chem. Soc.* **2009**, *131*, 15939-15944.
31. Pan, F.; Li, B.; Xiang, X.; Wang, G.; Li, Y., Efficient CO₂ Electroreduction by Highly Dense and Active Pyridinic Nitrogen on Holey Carbon Layers with Fluorine Engineering. *ACS Catal.* **2019**, *9*, 2124-2133.
32. Lin, Z.; Waller, G.; Liu, Y.; Liu, M.; Wong, C.-P., Facile Synthesis of Nitrogen-Doped Graphene via Pyrolysis of Graphene Oxide and Urea, and its Electrocatalytic Activity toward the Oxygen-Reduction Reaction. *Adv. Energy Mater.* **2012**, *2*, 884-888.

33. Hu, C.; Bai, S.; Gao, L.; Liang, S.; Yang, J.; Cheng, S.-D.; Mi, S.-B.; Qiu, J., Porosity-Induced High Selectivity for CO₂ Electroreduction to CO on Fe-Doped ZIF-Derived Carbon Catalysts. *ACS Catal.* **2019**, *9*, 11579-11588.
34. Zhu, Y.; Murali, S.; Stoller, M. D.; Ganesh, K. J.; Cai, W.; Ferreira, P. J.; Pirkle, A.; Wallace, R. M.; Cychoz, K. A.; Thommes, M.; Su, D.; Stach, E. A.; Ruoff, R. S., Carbon-Based Supercapacitors Produced by Activation of Graphene. *Science* **2011**, *332*, 1537-1541.
35. Bi, W.; Li, X.; You, R.; Chen, M.; Yuan, R.; Huang, W.; Wu, X.; Chu, W.; Wu, C.; Xie, Y., Surface Immobilization of Transition Metal Ions on Nitrogen-Doped Graphene Realizing High-Efficient and Selective CO₂ Reduction. *Adv. Mater.* **2018**, *30*, 1706617.
36. Hou, P.; Song, W.; Wang, X.; Hu, Z.; Kang, P., Well-Defined Single-Atom Cobalt Catalyst for Electrocatalytic Flue Gas CO₂ Reduction. *Small* **2020**, *16*, 2001896.
37. Zhang, N.; Zhou, T.; Chen, M.; Feng, H.; Yuan, R.; Zhong, C. a.; Yan, W.; Tian, Y.; Wu, X.; Chu, W.; Wu, C.; Xie, Y., High-Purity Pyrrole-Type FeN₄ Sites as a Superior Oxygen Reduction Electrocatalyst. *Energy Environ. Sci.* **2020**, *13*, 111-118.
38. Pan, F.; Liang, A.; Duan, Y.; Liu, Q.; Zhang, J.; Li, Y., Self-Growth-Templating Synthesis of 3D N,P,Co-doped Mesoporous Carbon Frameworks for Efficient Bifunctional Oxygen and Carbon Dioxide Electroreduction. *J. Mater. Chem. A* **2017**, *5*, 13104-13111.
39. Genovese, C.; Schuster, M. E.; Gibson, E. K.; Gianolio, D.; Posligha, V.; Grau-Crespo, R.; Cibin, G.; Wells, P. P.; Garai, D.; Solokha, V.; Krick Calderon, S.; Velasco-Velez, J. J.; Ampelli, C.; Perathoner, S.; Held, G.; Centi, G.; Arrigo, R., Operando Spectroscopy Study of the Carbon Dioxide Electro-Reduction by Iron Species on Nitrogen-Doped Carbon. *Nat. Commun.* **2018**, *9*, 935.

40. Chen, Y.; Ji, S.; Wang, Y.; Dong, J.; Chen, W.; Li, Z.; Shen, R.; Zheng, L.; Zhuang, Z.; Wang, D.; Li, Y., Isolated Single Iron Atoms Anchored on N-Doped Porous Carbon as an Efficient Electrocatalyst for the Oxygen Reduction Reaction. *Angew. Chem. In. Ed.* **2017**, *56*, 1-6.
41. Pan, F.; Yang, Y., Designing CO₂ Reduction Electrode Materials by Morphology and Interface Engineering. *Energy Environ. Sci.* **2020**, *13*, 2275-2309.
42. Tripkovic, V.; Vanin, M.; Karamad, M.; Björketun, M. E.; Jacobsen, K. W.; Thygesen, K. S.; Rossmeisl, J., Electrochemical CO₂ and CO Reduction on Metal-Functionalized Porphyrin-like Graphene. *J. Phys. Chem. C* **2013**, *117*, 9187-9195.
43. Zhu, G.; Li, Y.; Zhu, H.; Su, H.; Chan, S. H.; Sun, Q., Curvature-Dependent Selectivity of CO₂ Electrocatalytic Reduction on Cobalt Porphyrin Nanotubes. *ACS Catal.* **2016**, *6*, 6294-6301.
44. Cui, X.; An, W.; Liu, X.; Wang, H.; Men, Y.; Wang, J., C₂N-Graphene Supported Single-Atom Catalysts for CO₂ Electrochemical Reduction Reaction: Mechanistic Insight and Catalyst Screening. *Nanoscale* **2018**, *10*, 15262-15272.
45. Wang, L.; Higgins, D. C.; Ji, Y.; Morales-Guio, C. G.; Chan, K.; Hahn, C.; Jaramillo, T. F., Selective Reduction of CO to Acetaldehyde with CuAg Electrocatalysts. *Proc. Natl. Acad. Sci. U. S. A.* **2020**, *117*, 12572-12575.
46. Huan, T. N.; Ranjbar, N.; Rousse, G.; Sougrati, M.; Zitolo, A.; Mougel, V.; Jaouen, F.; Fontecave, M., Electrochemical Reduction of CO₂ Catalyzed by Fe-N-C Materials: A Structure-Selectivity Study. *ACS Catal.* **2017**, *7*, 1520-1525.

47. Ren, W.; Tan, X.; Yang, W.; Jia, C.; Xu, S.; Wang, K.; Smith, S. C.; Zhao, C., Isolated Diatomic Ni-Fe Metal–Nitrogen Sites for Synergistic Electroreduction of CO₂. *Angew. Chem. In. Ed.* **2019**, *58*, 6972-6976.
48. Pan, F.; Li, B.; Sarnello, E.; Hwang, S.; Gang, Y.; Feng, X.; Xiang, X.; Adli, N. M.; Li, T.; Su, D.; Wu, G.; Wang, G.; Li, Y., Boosting CO₂ Reduction on Fe-N-C with Sulfur Incorporation: Synergistic Electronic and Structural Engineering. *Nano Energy* **2020**, *68*, 104384.
49. Hussain, J.; Jónsson, H.; Skúlason, E., Calculations of Product Selectivity in Electrochemical CO₂ Reduction. *ACS Catal.* **2018**, *8*, 5240-5249.
50. Feng, Y.; An, W.; Wang, Z.; Wang, Y.; Men, Y.; Du, Y., Electrochemical CO₂ Reduction Reaction on M@Cu (211) Bimetallic Single-Atom Surface Alloys: Mechanism, Kinetics, and Catalyst Screening. *ACS Sustain. Chem. Eng.* **2020**, *8*, 210-222.
51. Peterson, A. A.; Abild-Pedersen, F.; Studt, F.; Rossmeisl, J.; Nørskov, J. K., How Copper Catalyzes the Electroreduction of Carbon Dioxide into Hydrocarbon Fuels. *Energ. Environ. Sci.* **2010**, *3*, 1311.
52. Lin, L.; Li, H.; Yan, C.; Li, H.; Si, R.; Li, M.; Xiao, J.; Wang, G.; Bao, X., Synergistic Catalysis over Iron-Nitrogen Sites Anchored with Cobalt Phthalocyanine for Efficient CO₂ Electroreduction. *Adv. Mater.* **2019**, *31*, 1903470.
53. Li, X.; Bi, W.; Chen, M.; Sun, Y.; Ju, H.; Yan, W.; Zhu, J.; Wu, X.; Chu, W.; Wu, C.; Xie, Y., Exclusive Ni–N₄ Sites Realize Near-Unity CO Selectivity for Electrochemical CO₂ Reduction. *J. Am. Chem. Soc.* **2017**, *139*, 14889-14892.

54. Pan, F.; Li, B.; Deng, W.; Du, Z.; Gang, Y.; Wang, G.; Li, Y., Promoting Electrocatalytic CO₂ Reduction on Nitrogen-Doped Carbon with Sulfur Addition. *Appl. Catal. B* **2019**, *252*, 240-249.
55. Dronskowski, R.; Bloechl, P. E., Crystal Orbital Hamilton Populations (COHP): Energy-Resolved Visualization of Chemical Bonding in Solids Based on Density-Functional Calculations. *J. Phys. Chem. C* **1993**, *97*, 8617-8624.
56. Chen, Z.; Song, Y.; Cai, J.; Zheng, X.; Han, D.; Wu, Y.; Zang, Y.; Niu, S.; Liu, Y.; Zhu, J.; Liu, X.; Wang, G., Tailoring the d-Band Centers Enables Co₄N Nanosheets to Be Highly Active for Hydrogen Evolution Catalysis. *Angew. Chem. In. Ed.* **2018**, *57*, 5076-5080.

TOC Graphic

